

Reversible canted persistent spin textures with large spin splitting in two-dimensional ferroelectric bilayer WTe_2

Moh. Adhib Ulil Absor and Iman Santoso

*Departement of Physics, Faculty of Mathematics and Natural Sciences,
Universitas Gadjah Mada, Sekip Utara BLS 21 Yogyakarta 55186 Indonesia.**

(Dated: August 12, 2022)

arXiv:2208.05902v1 [cond-mat.str-el] 11 Aug 2022

Abstract

The recent discovery of materials hosting persistent spin texture (PST) opens an avenue for the realization of energy-saving spintronics since they support an extraordinarily long spin lifetime. However, the stability of the PST is sensitively affected by symmetry breaking of the crystal induced by external perturbation such as the electric field. In this paper, through first-principles calculations supplemented by symmetry analysis, we report the emergence of the robust and stable PST with large spin splitting in the two-dimensional ferroelectric bilayer WTe_2 . Due to the low symmetry of the crystal (C_s point group), we observe a canted PST in the spin-split bands around the Fermi level displaying a unidirectional spin configuration tilted along the yz plane in the first Brillouin zone. Such a typical PST can be effectively reversed by out-of-plane ferroelectric switching induced by interlayer sliding along the in-plane direction. We further demonstrated that the reversible PST is realized by the application of an out-of-plane external electric field. Thus, our findings uncover the possibility of an electrically tunable PST in the 2D materials, offering a promising platform for highly efficient spintronics devices.

I. INTRODUCTION

The next generation of spintronics relies on the effective control and manipulation of an electron's spin degree of freedom without an additional external magnetic field, which is achievable by utilizing the effect of spin-orbit coupling (SOC)[1]. Many intriguing SOC-related phenomena were discovered, including spin relaxation [2, 3], spin Hall effect [4], spin galvanic effect [5], and spin ballistic transport [6]. In non-magnetic systems lacking inversion symmetry, the SOC induces momentum k -dependent spin-orbit field (SOF) that lifts Kramer's spin degeneracy and results in chiral spin polarization characterized by the spin-momentum-locking property as manifested by the Dresselhaus [7] and Rashba [8] effects. The Dresselhaus effect is generally observed on a system holding bulk inversion asymmetries such as bulk zinc blende [7] and wurtzite [9] semiconductors. On the other hand, the Rashba effect is associated with heterostructures and surfaces due to two-dimensional (2D) structural inversion asymmetry, as widely observed on semiconductor quantum-well (QW) [10, 11], surface heavy metal [12, 13], and several 2D-layered compounds [14–18].

* adib@ugm.ac.id

Recently, ferroelectric Rashba materials (FRMs) have stimulated the interest of researchers due to the reversible spontaneous polarization and the inherent Rashba effect [19–21]. Here, reversible Rashba spin textures can be achieved in a non-volatile way by switching the direction of the ferroelectric polarization [19], which is promising for electrically controllable spintronic devices [20–22]. α -GeTe was the first FRM predicted [23], and its reversible spin texture by switching ferroelectric polarization has been experimentally confirmed [24, 25]. After that, a handful of ferroelectric materials ranging from similar metal chalcogenides (SnTe) to metal-organic halide perovskites, such as (FA)SnI₃ [26], hexagonal semiconductors (LiZnSb) [27], and perovskite oxides (HfO₂ [28], and BiAlO₃ [29], were proposed to be FRMs. Despite the robust ferroelectricity, the strong SOC in these materials makes them promising for the realization of FRM-based spintronics devices. However, the strong SOC may induce fast spin decoherence through the Dyakonov-Perel (DP) mechanism [30], reducing spin lifetime, and hence limiting the performance of potential spintronic devices.

More recently, 2D ferroelectric materials with in-plane electric polarization have been proposed to eliminate the problem of spin dephasing [31–39]. Here, the SOC leads to a unidirectional out-of-plane spin configuration, resulting in the unidirectional out-of-plane SOF that is independent of the electron’s momentum. Such a typical spin configuration leads to the well-known persistent spin texture (PST) as was firstly proposed by Schliemann et al. [40], which could support an extraordinarily long spin lifetime of carriers [41, 42]. Previously, the PST has been demonstrated on semiconductor quantum-well (QW) having equal strength to the Dresselhaus and Rashba SOC [41, 43, 44] or on [110]-oriented semiconductor QWs in which the SOC is described by the [110] Dresselhaus model [41]. Recently, various 2D ferroelectric materials supporting the PST have been theoretically reported including WO₂Cl₂ [31], GaXY (X =Se, Te; Y =Cl, Br, I) [37, 38], hybrid perovskite benzyl ammonium lead-halide [39], and group-IV monochalcogenide [32–36]. However, considering the nature of the in-plane ferroelectricity in these materials, the presence of the PST may be broken due to the disturbing of the in-plane ferroelectricity, for instant, through the application of an external out-of-plane electric field [32, 45], thus hindering their practical spintronics. Therefore, finding novel 2D ferroelectric materials with robust and stable PST under the external electric field is highly desirable for practical purposes.

In this paper, we report the emergence of robust and stable PST with large spin splitting

in the two-dimensional ferroelectric bilayer WTe_2 . Recently, it has been reported that the bilayer WTe_2 is semimetal exhibiting interlayer sliding ferroelectricity [46–50], thus achieving the stable PST is expected to be useful for non-volatile spintronics. By performing first-principles density-functional theory (DFT) calculations, we show that the PST is observed in the spin-split states near the Fermi level having large spin splitting. We observed a uniform spin configuration in the substantially large region in the FBZ, which is unidirectionally tilted along the yz plane. Such a peculiar PST dubbed canted PST, which is strongly different from the previously discovered PST reported on conventional semiconductor QW [41, 43, 44] and 2D material systems with in-plane ferroelectricity [31–39]. By using $\vec{k} \cdot \vec{p}$ -based symmetry analysis, we clarified that the canted PST observed in the present systems is enforced by the out-of-plane mirror M_{yz} symmetry of the C_s point group. More importantly, we found that this typical PST can be effectively reversed upon ferroelectric switching, which is demonstrated through the application of an out-of-plane external electric field. Therefore, our study suggested that an electrically controllable PST in the present system for spintronics is plausible.

II. COMPUTATIONAL DETAILS

We have performed first-principles DFT calculations based on norm-conserving pseudo-potentials and optimized pseudo-atomic localized basis functions implemented in the OpenMX code [51–53]. The exchange-correlation functional was treated within generalized gradient approximation by Perdew, Burke, and Ernzerhof (GGA-PBE) [54, 55]. The basis functions were expanded by a linear combination of multiple pseudo atomic orbitals (PAOs) generated using a confinement scheme [52, 56], where three s -, three p -, two d -character numerical PAOs were used. The accuracy of the basis functions, as well as pseudo-potentials we used, were carefully bench-marked by the delta gauge method [57].

We used a periodic slab to model the bilayer WTe_2 , where a sufficiently large vacuum layer (25 Å) was applied to avoid the spurious interaction between slabs. We used a $12 \times 10 \times 1$ k -point and real space grids corresponding to energy cutoffs larger than 300 Ry to obtain the converged results of the self-consistent field (SCF) loops. The minimum-energy pathways of ferroelectric transitions were evaluated by using nudged elastic band (NEB) method based on the interatomic forces and total energy calculations [58]. We adopted the modern theory

of polarization based on the Berry phase (BP) method [59] to calculate the ferroelectric polarization. We considered a uniform external electric field perpendicular to the 2D plane of the crystal modeled by a sawtooth waveform during the SCF calculation and geometry optimization. Here, the energy convergence criterion was set to 10^{-9} eV. The lattice and positions of the atoms were optimized until the Hellmann-Feynman force components acting on each atom were less than $1 \text{ meV}/\text{\AA}$.

To evaluate the spin-splitting-related properties, we performed non-collinear DFT calculations, where the SOC was included self consistently in all calculations by using j -dependent pseudo potentials [60]. We calculated the spin textures by deducing the spin vector components (S_x, S_y, S_z) in the reciprocal lattice vector \vec{k} from the spin density matrix. Here, by using the spinor Bloch wave function, $\Psi_\mu^\sigma(\vec{r}, \vec{k})$, obtained from the OpenMX calculations after the SCF is achieved, we calculate the spin density matrix, $P_{\sigma\sigma'}(\vec{k}, \mu)$, through the following relation [61],

$$\begin{aligned}
 P_{\sigma\sigma'}(\vec{k}, \mu) &= \int \Psi_\mu^\sigma(\vec{r}, \vec{k}) \Psi_{\mu'}^{\sigma'}(\vec{r}, \vec{k}) d\vec{r} \\
 &= \sum_n \sum_{i,j} [c_{\sigma\mu i}^* c_{\sigma'\mu' j} S_{i,j}] e^{i\vec{R}_n \cdot \vec{k}},
 \end{aligned}
 \tag{1}$$

where S_{ij} is the overlap integral of the i -th and j -th localized orbitals, $c_{\sigma\mu i(j)}$ is expansion coefficient, σ (σ') is the spin index (\uparrow or \downarrow), μ is the band index, and \vec{R}_n is the n -th lattice vector. This method has been successfully applied in our previous studies on various 2D materials [32, 33, 35, 37, 38, 62–64]

III. RESULTS AND DISCUSSION

A. Atomic structure, symmetry, and ferroelectricity

Figs. 1(a)-(b) show the crystal structures of bilayer WTe_2 corresponding to the first Brillouin zone [Fig. 1(c)]. The bilayer WTe_2 crystallizes in a layered orthorhombic structure (also known as the T_d phase) consisting of a van der Waals (vdW) stacking of two $1T'$ WTe_2 monolayers. Here, the tungsten (W) atoms are octahedrally coordinated by the telluride (Te) atoms and the W atoms form a slightly buckled zigzag chain due to the metallic bonding, resulting in a distortion of the Te octahedron around each Te atom [Fig. 1(b)]. Monolayer $1T'$ WTe_2 is centrosymmetric with C_{2h} point group that is generated by the following sym-

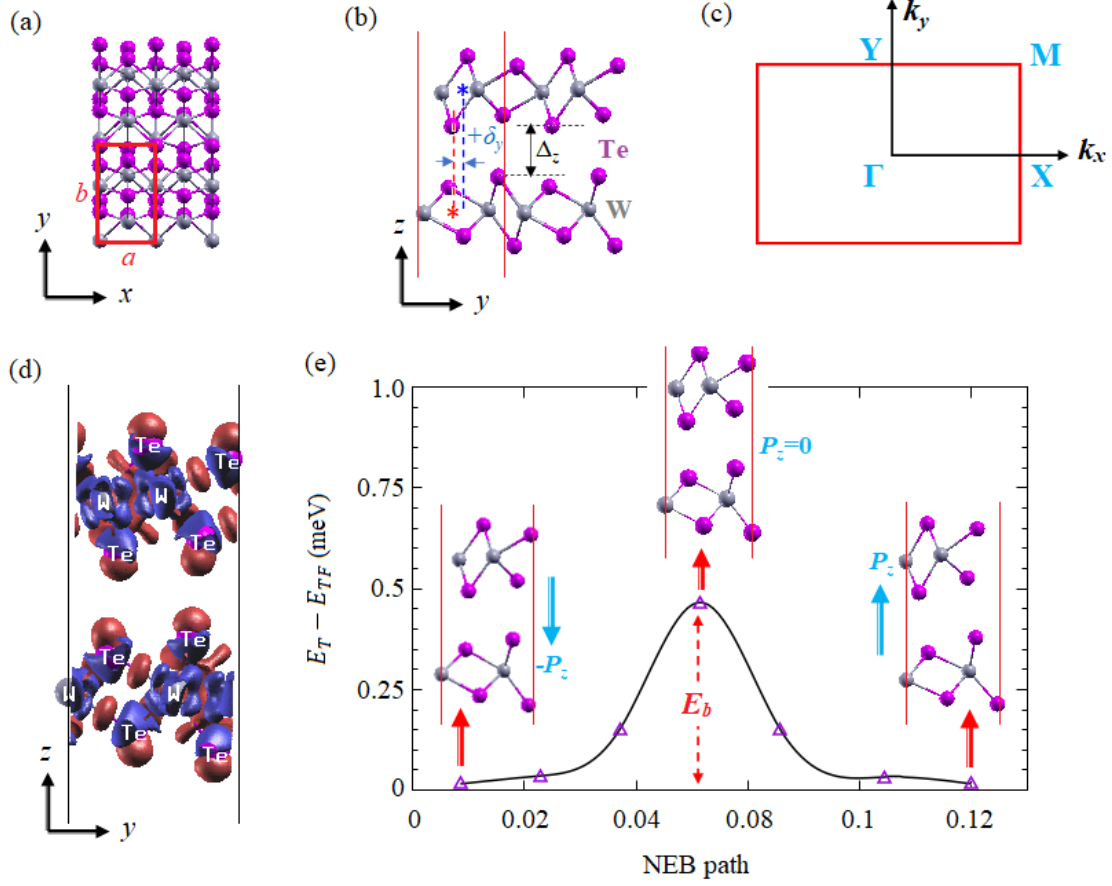


FIG. 1. (a)-(b) Atomic structures of bilayer WTe_2 viewed in the $x-y$ and $x-z$ planes, respectively, are presented. The unit cell of the crystal is indicated by the red line and characterized by a and b lattice parameters in the x and y directions, respectively. δ_y is the in-plane shift along the y direction between the upper and lower layers with respect to the inversion center as indicated by the dashed red and blue lines, while Δ_z indicates the interlayer out-of-plane interlayer distance, respectively. (c) The first Brillouin zone of bilayer WTe_2 is shown, where high symmetry \vec{k} points (Γ , X , Y , and M) are shown. (d) The interlayer differential charge density of bilayer WTe_2 where red and blue isosurface indicates electron accumulation and depletion after layer stacking, respectively. (e) Minimum-energy pathway of the ferroelectric (FE) transition in bilayer WTe_2 calculated using Nudged elastic band (NEB) method is presented. E_b is the barrier energy defined as the difference between the total energy of the system (E_T) with respect to the total energy of the ferroelectric (E_{TF}). Two FE structures in the ground state with opposite directions of the out-of-plane electric polarization (P_z) and a paraelectric (PE) structure are inserted.

metry operations, inversion symmetry \mathcal{I} , a mirror symmetry M_{yz} perpendicular to the x axis, and a two-fold screw rotation symmetry \bar{C}_{2x} around the x axis [65]. In contrast, the vdW stacking in the bilayer structure breaks both the inversion \mathcal{I} and screw rotation \bar{C}_{2x} symmetries, thus the crystal symmetry of the bilayer WTe_2 becomes C_s point group [48]. We find that the optimized structure of the bilayer WTe_2 for a and b lattice parameters are 3.48 Å and 6.27 Å, respectively, which is in good agreement with the previous theoretical reports [48–50] and experiments [46, 47]. However, these values are slightly larger than that observed on the monolayer $1T'$ WTe_2 [65]. Due to the substantial difference between the a and b parameters, the crystal geometry of the bilayer WTe_2 is strongly anisotropic, implying that these materials have a strongly anisotropic mechanical response being subjected to the uniaxial strain along the x - and y -direction similar to that observed on group IV monochalcogenide [34, 66, 67].

The low symmetry of the bilayer WTe_2 plays an important role in generating the out-of-plane ferroelectricity. Here, the absence of both the inversion \mathcal{I} and glide in-plane mirror \bar{M}_{xy} symmetries in the bilayer WTe_2 induces a small in-plane shift ($\Delta_y = 2\delta_y$) between adjacent layers along the y axis (known as in-plane interlayer sliding) [46–50], where δ_y is the in-plane shift along the y -direction between the upper and lower layers with respect to the inversion center as shown by the dashed red and blue lines in Fig. 1(b). In our calculation, the in-plane shift Δ_y is found to be 0.51 Å, which is much smaller than that of the out-of-plane interlayer distance (Δ_z) of 3.19 Å, but is agree-well with the previously calculated results [48–50]. Accordingly, a net charge transfer between the upper and lower layer is allowed, which is expected to produce an interface dipole in the out-of-plane direction. This is, in fact, confirmed by our calculated results of differential charge density shown in Fig. 1(d), displaying a vertical polarity induced by the electron depletion (blue color) and accumulation (red color) at the interlayer interface.

To further clarify the robustness of the out-of-plane ferroelectricity in bilayer WTe_2 , we show in Fig. 1(e) the calculated results of the ferroelectric transition pathways obtained from the NEB calculation. We find that two opposite ferroelectric (FE) states with the opposite orientation of the out-of-plane electric polarization (P_z) are observed, which can be reversed by the in-plane shift (Δ_y) between adjacent layers, passing through an intermediate paraelectric (PE) state with $P_z = 0$ [see the insert of Fig. 1(e)]. The intermediate PE state in bilayer WTe_2 has a C_{2v} point group due to an additional in-plane glide mirror symmetry

\bar{M}_{xy} operation, an in-plane mirror symmetry operation M_{xy} followed by a translation along y by a fractional translation of $1/2a$, thus enforcing the vanishing of P_z . Through BP calculation, we found that the calculated P_z in the FE state is $3.3 \times 10^{11} e \text{ cm}^{-2}$, which is in good agreement with the previous experimental value [46, 47] and the calculated results [48–50]. Moreover, the transition pathway connecting the two opposite FE states through the PE state yields barrier energy of 0.45 meV [Fig. 1(e)], which is much smaller than that observed on the well-known ferroelectric BaTiO₃ [68], suggesting the feasibility of a ferroelectric switch under ambient conditions.

B. Electronic structure, spin splitting, and spin polarization

Fig. 2(a) shows the electronic band structure of bilayer WTe₂ calculated along the selected \vec{k} path in the FBZ [see Fig. 1(c)] obtained without (black lines) and with (magenta lines) the SOC. One can see that four main edge states are crossing the Fermi level along the $X - \Gamma$ line, i.e., two-highest occupied and two-lowest unoccupied bands, resulting in a semi-metallic character of the bilayer WTe₂. Our calculated results of the density of states projected to the atomic orbitals confirmed that these edge bands mainly originated from the contribution of W- d_{xz} and Te- p_x orbitals [Fig. 2(b)]. From the symmetry point of view, these orbitals are invariant under M_{yz} mirror symmetry, and are consistent with the irreducible representations (IRs) \mathcal{A}_g (mostly of metal d orbital in the conduction) and \mathcal{B}_u (p orbital of content in the valence) in the C_s point group. Taking into account the SOC, these edge bands undergo a significant spin splitting due to the lack of inversion symmetry. In particular, we identify large splitting bands at the two-lowest unoccupied states as highlighted by pair bands (1) and (2) shown in Fig. 2(c)], which is driven by the contribution of the strong hybridization between the W- d_{xz} and Te- p_x orbitals [Fig. 2(b)]. Moreover, by mapping the spin-splitting energy projected to the FBZ, we found that the splitting energy up to 0.09 eV and 0.12 eV is observed on the pair bands (1) and (2), respectively, at the \vec{k} along the $X - \Gamma$ line [Figs. 2(d)-(e)]. These values are comparable to that observed on various 2D ferroelectric systems including group IV monochalcogenides (0.02 - 0.3 eV) [32–35] and GaXY ($X=\text{Se, Te; } Y=\text{Cl, Br, I}$) family (0.25 eV) [38], which is certainly sufficient to ensure the proper function of spintronic devices operating at room temperature. In addition, we also identify the strong anisotropy of the spin-splitting energy as clearly shown by the spin-splitting energy map in

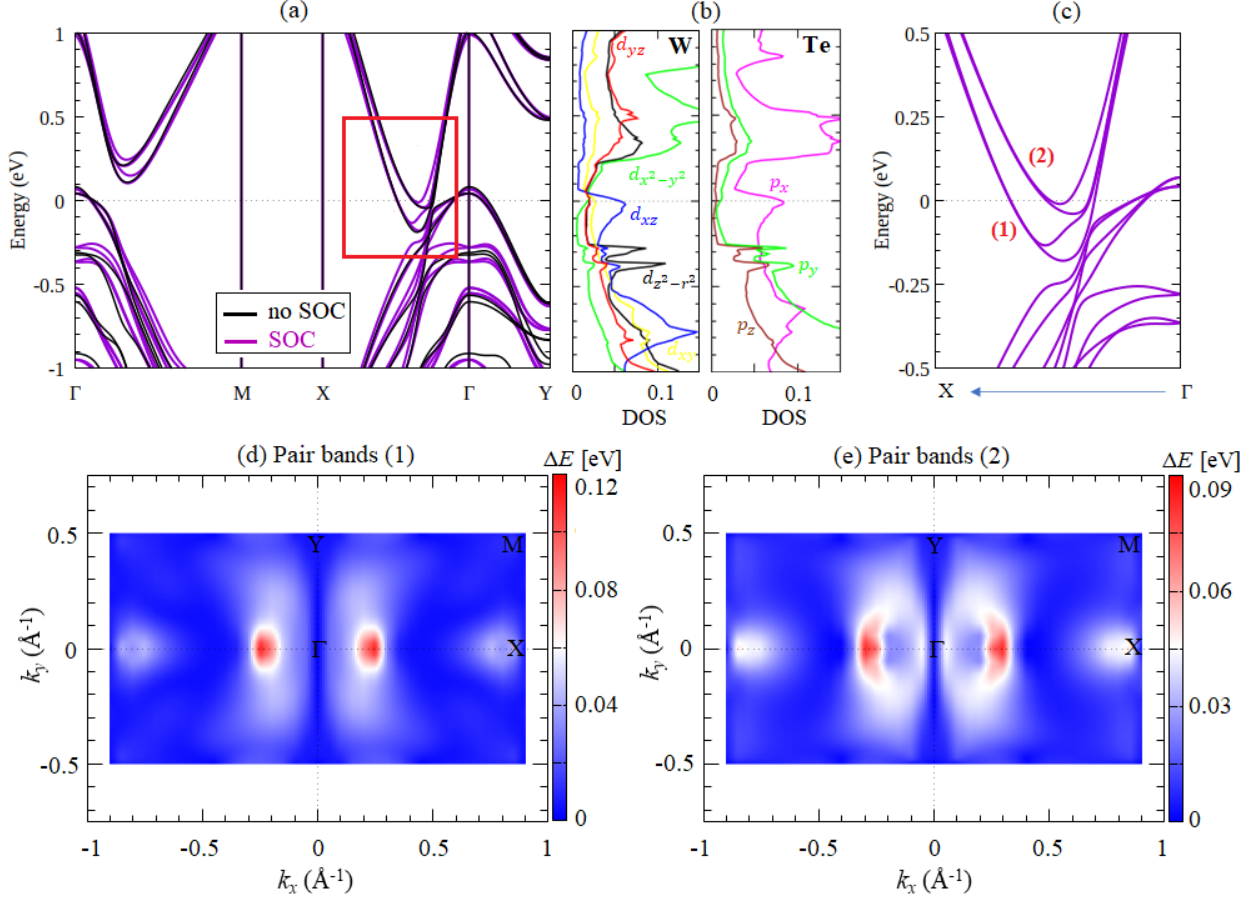


FIG. 2. (a) Band structure of bilayer WTe_2 calculated without (black lines) and with (magenta lines) the SOC are shown. (b) The density of states projected to the atomic orbitals for W and Te atoms are presented, where each orbital (p and d orbitals) is indicated by the different colors. (c) The spin-splitting bands of bilayer WTe_2 are calculated along the energy window highlighted by red lines in Fig. 2(a). Index (1) and (2) represent the two-lowest unoccupied pair bands near the Fermi level exhibiting the large spin-splitting energy. (d)-(e) Spin-splitting energy map projected to the first Brillouin zone calculated for pair bands (1) and (2), respectively, are shown. The magnitude of the spin-splitting energy, ΔE , defined as $\Delta E = |E(k, \uparrow) - E(k, \downarrow)|$, where $E(k, \uparrow)$ and $E(k, \downarrow)$ are the energy bands with up spin and down spin, respectively, is represented by the color scales.

Figs. 2(d)-(e)]. This anisotropic nature of the spin-splitting is enforced by the low symmetry of the crystal that is similar to that observed on various 2D group IV monochalcogenides [32–35] and GaXY ($X=\text{Se}, \text{Te}; Y=\text{Cl}, \text{Br}, \text{I}$) family [38].

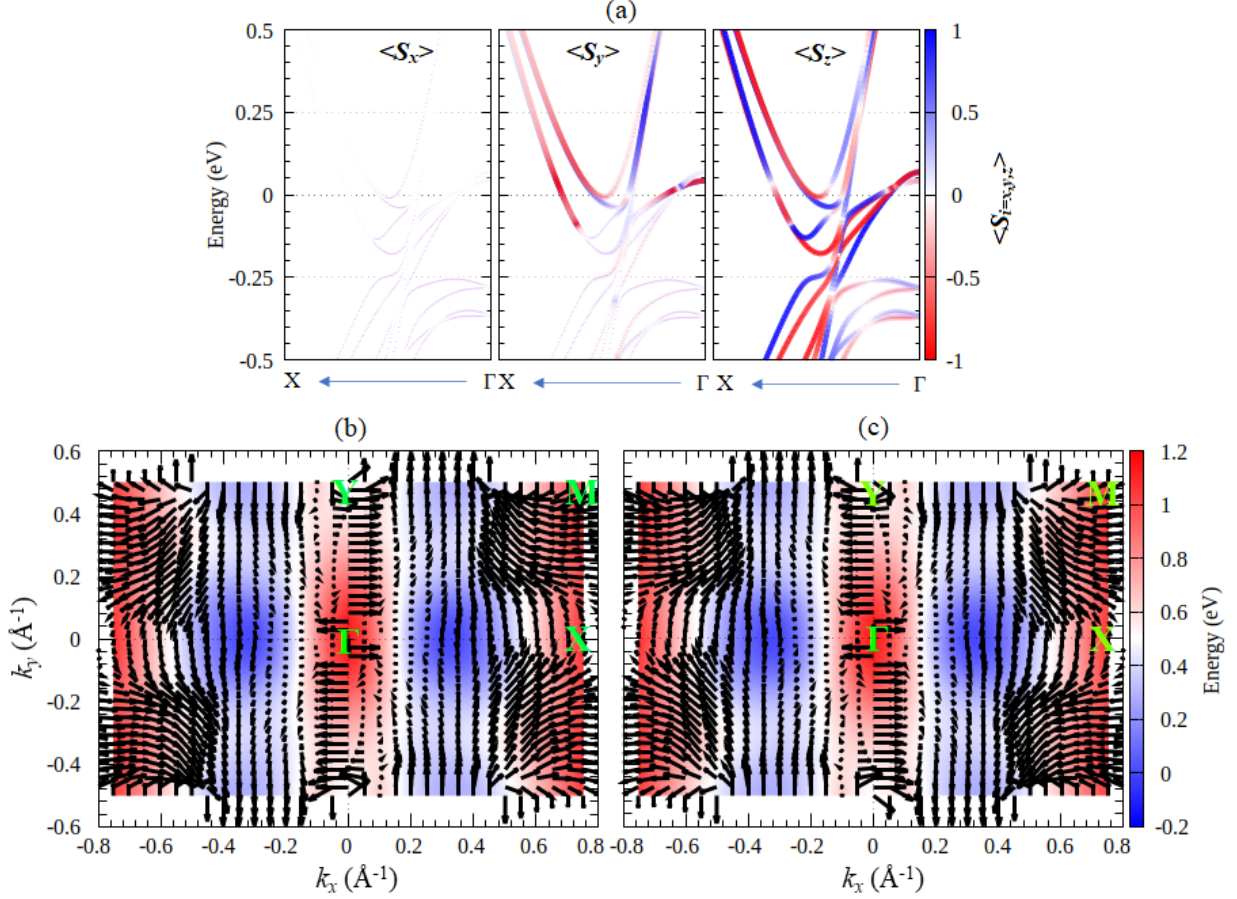


FIG. 3. (a) Spin-resolved projected to the spin-split bands near the Fermi level along the $X - \Gamma$ line where the expectation value of spin components ($\langle S_x \rangle$, $\langle S_y \rangle$, $\langle S_z \rangle$) represented by the color scale. (b)-(c) Spin texture projected to the first Brillouin zone calculated for the upper and lower bands in the pair bands (1), respectively, are shown. The black arrows represent the in-plane spin components of the spin polarization, while the color scale indicates the energy level of the bands.

To further characterize the spin-splitting properties, we focused on the spin-split states near the band edges around the Fermi level along the $X - \Gamma$ line due to their significant role in the transport properties. The calculated result of spin-resolved projected to the bands along the $X - \Gamma$ line is displayed in Fig. 3(a). Due to the presence of the M_{yz} mirror plane in the bilayer WTe_2 , the spin polarization has no x -component of spin (S_x), but exhibits a significant y - and z -components of spin (S_y , S_z), indicating that the spin polarizations are tilted along the yz plane in the FBZ. By calculating the k -space spin textures for the upper and lower bands [Figs. 3(c) and 3(d), respectively] in the spin-split pair bands (1) [see Fig.

2(c)], we observe a unidirectional spin configuration that is visible at the substantially large region in the FBZ. Such a tilting and unidirectional spin configuration in the k -space lead to the formation of the canted PST, which differs strongly from the well-known PST induced by the balancing of the Rashba and Dresselhaus SOCs [41, 43, 44] or described by the [110] Dresselhaus model [41] as widely observed on various semiconductor QW [43, 44]. The observed canted PST in the present system is expected to induce unidirectional canted SOF in the k -space, protecting the spin from decoherence through suppressing the Dyakonov-Perel spin-relaxation [40, 41]. Accordingly, an extremely long spin lifetime is expectable [40–42], offering a promising platform to realize an efficient spintronics device.

To understand the nature of the observed canted PST, we consider a symmetry-based $\vec{k} \cdot \vec{p}$ Hamiltonian model similarly used in recent works [65, 69–71]. Since the electronic states near the Fermi level around the Γ point belongs to the IRs \mathcal{A}_g (d orbital) and \mathcal{B}_u (p orbital) of the C_s point group, one can construct the following $\vec{k} \cdot \vec{p}$ Hamiltonian:

$$\mathcal{H}_\Gamma = \mathcal{H}_0 + \mathcal{H}_{SOC} \quad (2)$$

where the first term describes the spinless part of the Hamiltonian:

$$\mathcal{H}_0 = m_p k^2 \sigma_0 \tau_0 + (m_d k^2 + \delta) \sigma_0 \tau_z + \beta k_y \sigma_0 \tau_y + \gamma \sigma_0 \tau_x. \quad (3)$$

Here, τ_i (σ_i) with $i = x, y, z$ and τ_0 (σ_0) are the Pauli matrices and identity matrix working in the orbital (spin) space, respectively, and $m_{p(d)}$ is the effective mass of the occupied (unoccupied) bands. β , γ , and δ are the parameter representing the degree of the crystalline anisotropy between k_x and k_y , the breaking of the inversion symmetry, and the degree of the band inversion, respectively. The second term in Eq. (2) represents the SOC term which can be written in the first order in k as

$$\mathcal{H}_{SOC} = (\alpha_1 k_x \sigma_y + \alpha_2 k_y \sigma_x + \alpha_3 k_x \sigma_z) \tau_x, \quad (4)$$

where α_1 , α_2 , and α_3 are the SOC parameters. Eq. (4) is the symmetry-allowed SOCs obtained by considering the mirror symmetry $M_{yz} = i\sigma_x \tau_0$ and time reversal symmetry $\mathcal{T} = i\sigma_y \mathcal{K}$, where $\mathcal{T}^2 = -1$ for the spinor and \mathcal{K} is the complex conjugation.

By focusing on the spin-split states along the $\Gamma - X$ line ($k_y = 0$), the following simplified Hamiltonian holds,

$$\mathcal{H}_{\Gamma-X} = m_p k_x^2 \sigma_0 \tau_0 + (m_d k_x^2 + \delta) \sigma_0 \tau_z + \gamma \sigma_0 \tau_x + (\alpha_1 k_x \sigma_y + \alpha_3 k_x \sigma_z) \tau_x. \quad (5)$$

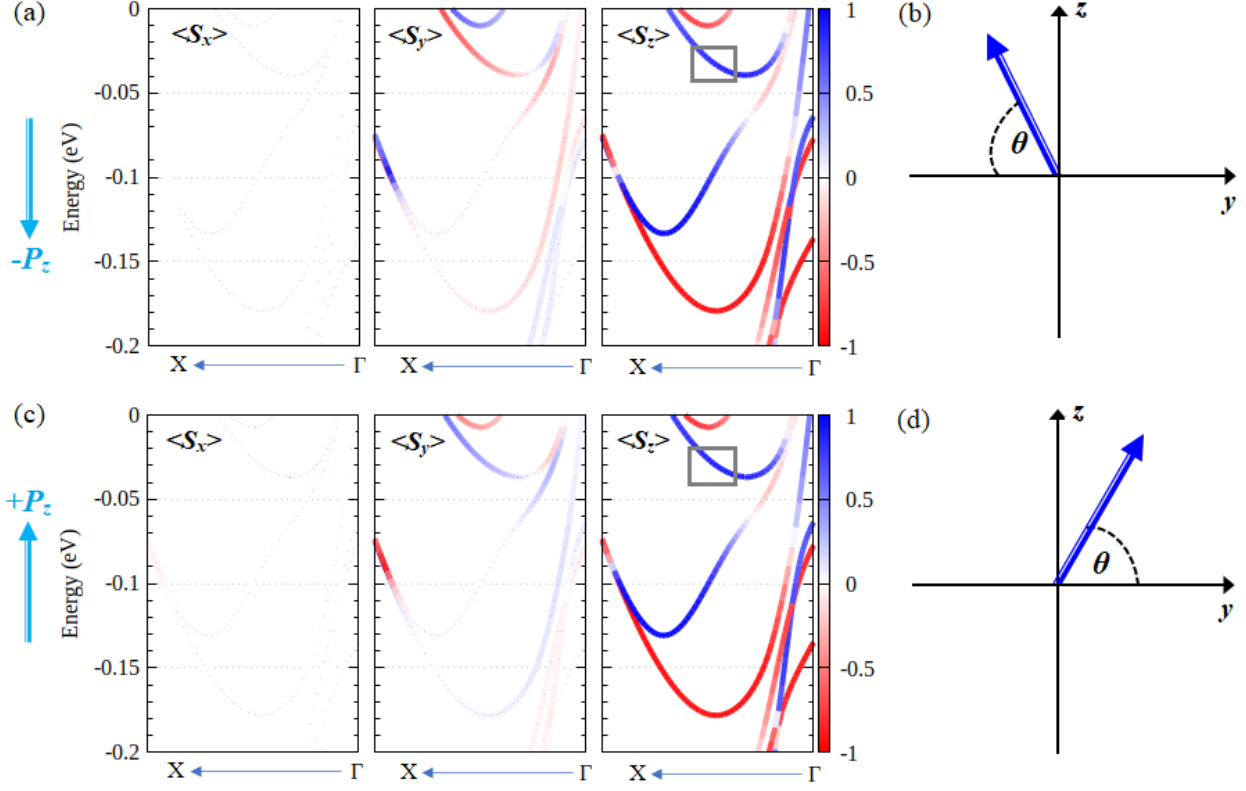


FIG. 4. Relation between the out-of-plane ferroelectric polarization P_z and the spin polarization. (a) Spin-resolved projected bands for the bilayer WTe_2 having $-P_z$ orientation of the electric polarization and (b) the schematic view of the canted PST are shown. The canted PST is evaluated for the spin polarization at a certain k as indicated by the black line. (c)-(d) Same with Figs. 4(a)-(b) but for the bilayer WTe_2 with $+P_z$ orientation of the electric polarization. The expectation value of spin components ($\langle S_x \rangle$, $\langle S_y \rangle$, $\langle S_z \rangle$) are represented by the color scale.

From the last two terms of Eq. (5), it is obvious that the spin textures should be unidirectionally tilted along the yz plane, which is agree-well with the observed spin-resolved bands shown in Fig. 3(a) and the k -space spin texture presented in Figs. 3(b)-(c). Moreover, the SOC parameters (α_1 , α_3), which are important for spintronics device operations, can be evaluated by fitting the energy dispersion obtained from the solution of Eq. (5) to the DFT energy bands along the $\Gamma - X$. For the lowest unoccupied bands [see the pair bands (1) in Fig. 2(c)], we find that the calculated SOC parameters are $0.09 \text{ eV}\text{\AA}$ and $1.15 \text{ eV}\text{\AA}$ for α_1 and α_3 , respectively. These values are much larger than that observed on various semiconductor QW [43, 44].

C. Reversible Canted PST

To enrich the physics and possible application of the present systems, we examine the correlation between the observed canted PST and ferroelectricity. Here, an interesting property known as reversible canted PST holds, i.e., the orientation of the unidirectional tilted spin configuration is reversed by switching the direction of the out-of-plane spontaneous electric polarization P_z . Fig. 4 displays the evolution of the spin-resolved bands near the Fermi level along the $X - \Gamma$ line in the bilayer WTe_2 under the different orientation of the out-of-plane ferroelectric polarization P_z . Interestingly, when the direction of P_z is reversed, the out-of-plane spin component (S_z) is invariant, while the in-plane spin component S_y is reversed simultaneously [Figs. 4(a) and 4(c)]. As a result, a reversible canted PST is achieved as schematically shown in Figs. 4(b) and 4(c). Such a reversible PST offers a promising platform to realize a non-volatile control of the PST through the application of the external electric field, which is useful for spintronics devices implementing spin Hall effect [20–22].

The physical mechanism behind the reversible canted PST can be understood in terms of symmetry analysis. Let us consider a general symmetry operator $g = \left\{ \Omega | \vec{t}_R \right\}$, where Ω is point group symmetry operation and \vec{t}_R is the translation vector operator. Since the spin polarization vector $\vec{S}(\vec{k})$ is a time-reversal pseudovector, for a given symmetry operator g , the $\vec{S}(\vec{k})$ can be transformed by the relation $\vec{S}'(\vec{k}) = g\vec{S}(\vec{k}) = \mathcal{P}_R\mathcal{P}_t\vec{S}(\vec{k})$, where $\mathcal{P}_{R(t)}$ is the spatial (temporal) parity operator correlated with g . In particular, $\mathcal{P}_t = \pm 1$ when $\hat{\Omega}(\vec{k}) = \pm\vec{k} + \vec{G}$, where \vec{G} is the multiples of the reciprocal lattice vector. As for the bilayer WTe_2 , the reversal polarization (P_z) direction between the two FE states is related to the PE state having glide in-plane mirror symmetry \bar{M}_{xy} [see Fig. 1(d)], thus we obtained that $\mathcal{P}_R = -1$ and $\mathcal{P}_t = 1$. Accordingly, the reversal canted PST can also be correlated to \bar{M}_{xy} through the following transformation: $(S_y, S_z)^{+P_z} = (-S_y, S_z)^{-P_z}$. This shows that the canted PST is reversed as the sign of the S_y spin component is reversed, which is consistent with the observed spin-resolved bands and the spin textures are shown in Fig. 4.

We emphasized here that the reversible canted PST observed in the present study is the key for the nonvolatile spintronic applications. Here, the application of an electric field is an effective method to realize the reversible canted PST. Therefore, we introduce an external electric field (E_z) oriented perpendicular to the 2D surface (\hat{z} -direction), which

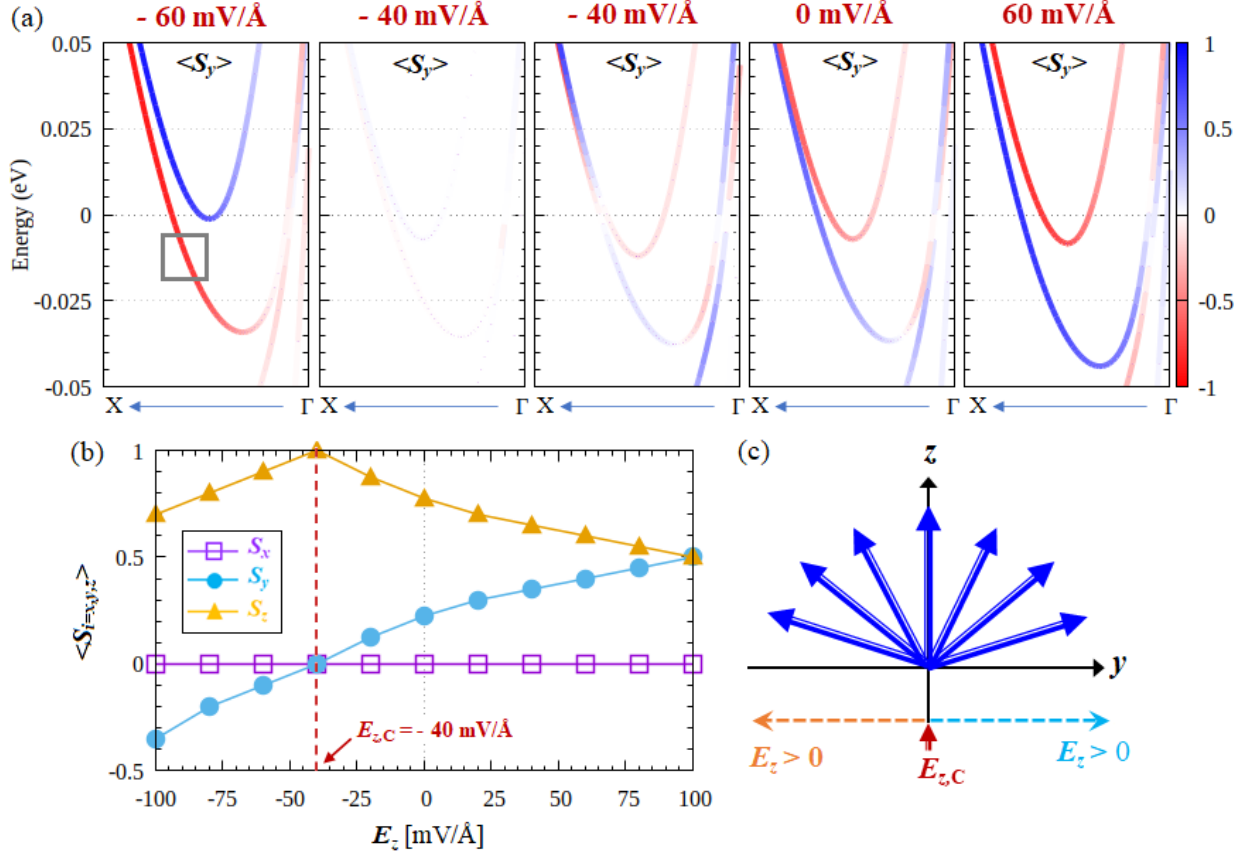


FIG. 5. (a) Evolution of the spin-resolved projected bands for the S_y spin component under the external out-of-plane electric field E_z is shown. (b) The dependence of the expectation value of spin on the electric field E_z calculated for the particular k point highlighted by the black line in Fig. 5(a) is presented. The critical electric field E_z^c showing the paraelectric state is identified. (c) A schematic illustration of the reversible canted PST is shown.

can be implemented through the application of a gate voltage [32, 45]. Since the reversible canted PST in bilayer WTe_2 depends on the sign of the S_y spin component [see Figs. 4(a) and 4(c)], we further show in Fig. 5(a) the modulation of the S_y under the different sign and magnitude of the electric field E_z . Obviously, we identify the reversible spin polarization as indicated by the reversal sign of the S_y under the switching direction of E_z . By calculating the spin polarization at the certain k [see the black line in Fig. 5(a) for the representation], the E_z -dependent of the expectation value of spin components (S_x , S_y , S_z) are presented in Fig. 5(b). When E_z is applied along the $+z$ direction, all the spin components have the same sign as that of the equilibrium system. However, the sign of the S_y becomes fully

reversed when $E_z > 40$ mV/Å is applied along the $-\hat{z}$ direction. At the electric field of -40 mV/Å, defining the critical field ($E_{z,c}$) applied along the $-\hat{z}$ direction, the PE state of the bilayer WTe₂ is achieved, thus the S_y becomes zero [Fig. 5(b)]. The switching sign of the S_y under the E_z indicates that an electrically reversible canted PST is achieved; see Fig. 5(c) for schematic representation, thus putting forward the bilayer WTe₂ as a promising candidate for efficient and nonvolatile spintronic devices.

Finally, we comment on the main difference of the PST found in the present system with that observed on various 2D materials with in-plane ferroelectricity such as WO₂Cl₂ [31], GaXY ($X=$ Se, Te; $Y=$ Cl, Br, I) [37, 38], hybrid perovskite benzyl ammonium lead-halide [39], and group-IV monochalcogenide [32–36]. In these materials, the spin textures are symmetrically driven by the in-plane mirror (or glide in-plane mirror) M_{xy} symmetry of the C_{2v} point group, leading to the fully out-of-plane PST that is similar to the [110]-Dresselhaus model observed in the semiconductor QW [41]. However, such a peculiar PST can be destroyed by breaking the M_{xy} through the application of the electric field perpendicular to the 2D material surface. In fact, the breaking of the PST by the electric field has been previously reported on 2D material group IV monochalcogenide, thus limiting the spintronics functionality. In contrast, for our systems, the canted PST is enforced by the out-of-plane mirror symmetry M_{yz} of the C_s point group. Since the M_{yz} is invariant under the out-of-plane electric field, the robust and stable PST is achieved [see Figs. 5(a)-(b)], thus the present system is more beneficial for spintronics applications.

IV. CONCLUSION

In summary, through first-principles DFT calculations supplemented by symmetry analysis, we have systematically investigated the SOC-related properties of the ferroelectric bilayer WTe₂, a novel 2D material having a coexistence between the ferroelectricity and semimetal property. We have observed the emergence of the novel type of PST in the spin-split states around the Fermi level, dubbed canted PST. This particular PST exhibits a unidirectional spin configuration tilted along the yz plane in the FBZ, which is significantly different from the previous PST widely observed in various semiconductor QW [41, 43, 44] and 2D material systems with in-plane ferroelectricity [31–39]. Our $\vec{k} \cdot \vec{p}$ -based symmetry analysis has clarified that the canted PST observed in the present systems is enforced by the out-of-plane

mirror M_{yz} symmetry of the C_s point group in the bilayer WTe_2 . More importantly, we have shown that this typical PST can be effectively reversed upon the out-of-plane ferroelectric switching, which has been demonstrated through the application of an out-of-plane external electric field. Therefore, our study suggested that the present system is promising for efficient and non-volatile spintronics devices.

Since the canted PST found in the present study is driven by the out-of-plane mirror symmetry M_{yz} operation in the C_s point group, it is expected that this typical PST can also be achieved on other 2D materials having the similar point group symmetry. Recently, there have been several other 2D bilayer systems that were predicted to maintain the interlayer sliding ferroelectricity and low symmetry of the crystals, such as ZrI_2 [72, 73] and VS_2 [74], thus opening a possibility to further explore the achievable PST in these materials. Our predictions are expected to stimulate further theoretical and experimental research in the exploration of PST-based 2D materials, widening the range of the 2D materials for future spintronic applications.

ACKNOWLEDGMENTS

This research was performed using the computer facilities at Universitas Gadjah Mada, Republic of Indonesia.

-
- [1] A. Manchon, H. C. Koo, J. Nitta, S. M. Frolov, and R. A. Duine, New perspectives for Rashba spin-orbit coupling, *Nat. Matter* **14**, 871 (2015).
 - [2] J. Fabian and S. D. Sarma, Spin relaxation of conduction electrons, *Journal of Vacuum Science & Technology B: Microelectronics and Nanometer Structures Processing, Measurement, and Phenomena* **17**, 1708 (1999).
 - [3] N. S. Averkiev and L. E. Golub, Giant spin relaxation anisotropy in zinc-blende heterostructures, *Phys. Rev. B* **60**, 15582 (1999).
 - [4] X.-L. Qi, Y.-S. Wu, and S.-C. Zhang, Topological quantization of the spin Hall effect in two-dimensional paramagnetic semiconductors, *Phys. Rev. B* **74**, 085308 (2006).
 - [5] S. D. Ganichev, E. L. Ivchenko, V. V. Bel'kov, S. A. Tarasenko, M. Sollinger, D. Weiss,

- W. Wegscheider, and W. Prettl, Spin-galvanic effect, *Nature* **417**, 153 (2002).
- [6] J. P. Lu, J. B. Yau, S. P. Shukla, M. Shayegan, L. Wissinger, U. Rössler, and R. Winkler, Tunable Spin-Splitting and Spin-Resolved Ballistic Transport in GaAs/AlGaAs Two-Dimensional Holes, *Phys. Rev. Lett.* **81**, 1282 (1998).
- [7] G. Dresselhaus, Spin-orbit coupling effects in zinc blende structures, *Phys. Rev.* **100**, 580 (1955).
- [8] E. I. Rashba, Properties of semiconductors with an extremum loop. 1. Cyclotron and combi-national resonance in a magnetic field perpendicular to the plane of the loop, *Sov. Phys. Solid State* **2**, 1224 (1960).
- [9] W.-T. Wang, C. L. Wu, S. F. Tsay, M. H. Gau, I. Lo, H. F. Kao, D. J. Jang, J.-C. Chiang, M.-E. Lee, Y.-C. Chang, C.-N. Chen, and H. C. Hsueh, Dresselhaus effect in bulk wurtzite materials, *Applied Physics Letters* **91**, 082110 (2007), <https://doi.org/10.1063/1.2775038>.
- [10] J. Nitta, T. Akazaki, H. Takayanagi, and T. Enoki, Gate control of spin-orbit interaction in an inverted $\text{In}_{0.53}\text{Ga}_{0.47}\text{As}/\text{In}_{0.52}\text{Al}_{0.48}\text{As}$ heterostructure, *Phys. Rev. Lett.* **78**, 1335 (1997).
- [11] A. D. Caviglia, M. Gabay, S. Gariglio, N. Reyren, C. Cancellieri, and J.-M. Triscone, Tunable rashba spin-orbit interaction at oxide interfaces, *Phys. Rev. Lett.* **104**, 126803 (2010).
- [12] S. LaShell, B. A. McDougall, and E. Jensen, Spin splitting of an au(111) surface state band observed with angle resolved photoelectron spectroscopy, *Phys. Rev. Lett.* **77**, 3419 (1996).
- [13] Y. M. Koroteev, G. Bihlmayer, J. E. Gayone, E. V. Chulkov, S. Blügel, P. M. Echenique, and P. Hofmann, Strong spin-orbit splitting on bi surfaces, *Phys. Rev. Lett.* **93**, 046403 (2004).
- [14] H. L. Zhuang, V. R. Cooper, H. Xu, P. Ganesh, R. G. Hennig, and P. R. C. Kent, Rashba effect in single-layer antimony telluroiodide sbte_i, *Phys. Rev. B* **92**, 115302 (2015).
- [15] Z. S. Popović, J. M. Kurdestany, and S. Satpathy, Electronic structure and anisotropic rashba spin-orbit coupling in monolayer black phosphorus, *Phys. Rev. B* **92**, 035135 (2015).
- [16] M. A. U. Absor, I. Santoso, Harsojo, K. Abraha, H. Kotaka, F. Ishii, and M. Saito, Strong rashba effect in the localized impurity states of halogen-doped monolayer ptse₂, *Phys. Rev. B* **97**, 205138 (2018).
- [17] Y. Affandi and M. A. Ulil Absor, Electric field-induced anisotropic rashba splitting in two dimensional tungsten dichalcogenides wx₂ (x: S, se, te): A first-principles study, *Physica E: Low-dimensional Systems and Nanostructures* **114**, 113611 (2019).
- [18] M. A. U. Absor, I. Santoso, Harsojo, K. Abraha, H. Kotaka, F. Ishii, and M. Saito, Polarity

- tuning of spin-orbit-induced spin splitting in two-dimensional transition metal dichalcogenides, *Journal of Applied Physics* **122**, 153905 (2017), <https://doi.org/10.1063/1.5008475>.
- [19] S. Picozzi, Ferroelectric rashba semiconductors as a novel class of multifunctional materials, *Frontiers in Physics* **2**, 10 (2014).
- [20] H. Wang, P. Gopal, S. Picozzi, S. Curtarolo, M. Buongiorno Nardelli, and J. Sławińska, Spin hall effect in prototype rashba ferroelectrics gete and snTe, *npj Computational Materials* **6**, 7 (2020).
- [21] S. Varotto, L. Nesi, S. Cecchi, J. Sławińska, P. Noël, S. Petrò, F. Fagiani, A. Novati, M. Cantoni, D. Petti, E. Albisetti, M. Costa, R. Calarco, M. Buongiorno Nardelli, M. Bibes, S. Picozzi, J.-P. Attané, L. Vila, R. Bertacco, and C. Rinaldi, Room-temperature ferroelectric switching of spin-to-charge conversion in germanium telluride, *Nature Electronics* **4**, 740 (2021).
- [22] A. Matos-Abiague and J. Fabian, Tunneling anomalous and spin hall effects, *Phys. Rev. Lett.* **115**, 056602 (2015).
- [23] D. Di Sante, P. Barone, R. Bertacco, and S. Picozzi, Electric control of the giant rashba effect in bulk gete, *Advanced Materials* **25**, 509 (2012).
- [24] M. Liebmann, C. Rinaldi, D. Di Sante, J. Kellner, C. Pauly, R. N. Wang, J. E. Boschker, A. Giussani, S. Bertoli, M. Cantoni, L. Baldrati, M. Asa, I. Vobornik, G. Panaccione, D. Marchenko, J. Sánchez-Barriga, O. Rader, R. Calarco, S. Picozzi, R. Bertacco, and M. Morgenstern, Giant rashba-type spin splitting in ferroelectric gete(111), *Advanced Materials* **28**, 560 (2016).
- [25] C. Rinaldi, S. Varotto, M. Asa, J. Sławińska, J. Fujii, G. Vinai, S. Cecchi, D. Di Sante, R. Calarco, I. Vobornik, G. Panaccione, S. Picozzi, and R. Bertacco, Ferroelectric control of the spin texture in gete, *Nano Letters* **18**, 2751 (2018).
- [26] A. Stroppa, D. Di Sante, P. Barone, M. Bokdam, G. Kresse, C. Franchini, M.-H. Whangbo, and S. Picozzi, Tunable ferroelectric polarization and its interplay with spin-orbit coupling in tin iodide perovskites, *Nature Communications* **5**, 5900 (2014).
- [27] A. Narayan, Class of rashba ferroelectrics in hexagonal semiconductors, *Phys. Rev. B* **92**, 220101 (2015).
- [28] L. L. Tao, T. R. Paudel, A. A. Kovalev, and E. Y. Tsymbal, Reversible spin texture in ferroelectric HfO₂, *Phys. Rev. B* **95**, 245141 (2017).
- [29] L. G. D. da Silveira, P. Barone, and S. Picozzi, Rashba-dresselhaus spin-splitting in the bulk

- ferroelectric oxide BiAlO_3 , Phys. Rev. B **93**, 245159 (2016).
- [30] M. I. Dyakonov and V. I. Perel, . spin relaxation of conduction electrons in noncentrosymmetric semiconductors, Sov. Phys. Solid State **13**, 3023 (1972).
- [31] H. Ai, X. Ma, X. Shao, W. Li, and M. Zhao, Reversible out-of-plane spin texture in a two-dimensional ferroelectric material for persistent spin helix, Phys. Rev. Materials **3**, 054407 (2019).
- [32] M. A. U. Absor, Y. Faishal, M. Anshory, I. Santoso, and F. Ishii, Highly persistent spin textures with giant tunable spin splitting in the two-dimensional germanium monochalcogenides, Journal of Physics: Condensed Matter **33**, 305501 (2021).
- [33] M. A. U. Absor and F. Ishii, Doping-induced persistent spin helix with a large spin splitting in monolayer SnSe , Phys. Rev. B **99**, 075136 (2019).
- [34] M. Anshory and M. A. U. Absor, Strain-controlled spin-splitting in the persistent spin helix state of two-dimensional SnSe monolayer, Physica E: Low-dimensional Systems and Nanostructures **124**, 114372 (2020).
- [35] M. A. U. Absor and F. Ishii, Intrinsic persistent spin helix state in two-dimensional group-iv monochalcogenide $m\text{x}$ monolayers ($m = \text{Sn}$ or Ge and $x = \text{S}$, Se , or Te), Phys. Rev. B **100**, 115104 (2019).
- [36] H. Lee, J. Im, and H. Jin, Emergence of the giant out-of-plane rashba effect and tunable nanoscale persistent spin helix in ferroelectric SnTe thin films, Applied Physics Letters **116**, 022411 (2020).
- [37] S. A. Sasmito, M. Anshory, I. Jihad, and M. A. U. Absor, Reversible spin textures with giant spin splitting in two-dimensional $\text{Ga}xy$ ($x = \text{Se}$, Te ; $y = \text{Cl}$, Br , I) compounds for a persistent spin helix, Phys. Rev. B **104**, 115145 (2021).
- [38] M. A. U. Absor and F. Ishii, Large band splitting with tunable spin polarization in the two-dimensional ferroelectric $\text{Ga}xy$ family ($x = \text{Se}$, Te ; $y = \text{Cl}$, Br , I), Phys. Rev. B **103**, 045119 (2021).
- [39] F. Jia, S. Hu, S. Xu, H. Gao, G. Zhao, P. Barone, A. Stroppa, and W. Ren, Persistent spin-texture and ferroelectric polarization in 2d hybrid perovskite benzylammonium lead-halide, The Journal of Physical Chemistry Letters **11**, 5177 (2020).
- [40] J. Schliemann, J. C. Egues, and D. Loss, Nonballistic spin-field-effect transistor, Phys. Rev. Lett. **90**, 146801 (2003).

- [41] B. A. Bernevig, J. Orenstein, and S.-C. Zhang, Exact $su(2)$ symmetry and persistent spin helix in a spin-orbit coupled system, *Phys. Rev. Lett.* **97**, 236601 (2006).
- [42] P. Altmann, M. P. Walser, C. Reichl, W. Wegscheider, and G. Salis, Suppressed decay of a laterally confined persistent spin helix, *Phys. Rev. B* **90**, 201306 (2014).
- [43] M. P. Walser, C. Reichl, W. Wegscheider, and G. Salis, Direct mapping of the formation of a persistent spin helix, *Nature Physics* **8**, 757 (2012).
- [44] A. Sasaki, S. Nonaka, Y. Kunihashi, M. Kohda, T. Bauernfeind, T. Dollinger, K. Richter, and J. Nitta, Direct determination of spin-orbit interaction coefficients and realization of the persistent spin helix symmetry, *Nature Nanotechnology* **9**, 703 (2014).
- [45] J. Sławińska, F. T. Cerasoli, P. Gopal, M. Costa, S. Curtarolo, and M. B. Nardelli, Ultrathin SnTe films as a route towards all-in-one spintronics devices, *2D Materials* **7**, 025026 (2020).
- [46] Z. Fei, W. Zhao, T. A. Palomaki, B. Sun, M. K. Miller, Z. Zhao, J. Yan, X. Xu, and D. H. Cobden, Ferroelectric switching of a two-dimensional metal, *Nature* **560**, 336 (2018).
- [47] P. Sharma, F.-X. Xiang, D.-F. Shao, D. Zhang, E. Y. Tsymbal, A. R. Hamilton, and J. Seidel, A room-temperature ferroelectric semimetal, *Science Advances* **5**, eaax5080 (2019).
- [48] H. Wang and X. Qian, Ferroelectric nonlinear anomalous hall effect in few-layer wte2, *npj Computational Materials* **5**, 119 (2019).
- [49] X. Liu, Y. Yang, T. Hu, G. Zhao, C. Chen, and W. Ren, Vertical ferroelectric switching by in-plane sliding of two-dimensional bilayer wte2, *Nanoscale* **11**, 18575 (2019).
- [50] Q. Yang, M. Wu, and J. Li, Origin of two-dimensional vertical ferroelectricity in wte2 bilayer and multilayer, *The Journal of Physical Chemistry Letters* **9**, 7160 (2018), <https://doi.org/10.1021/acs.jpcllett.8b03654>.
- [51] T. Ozaki, H. Kino, J. Yu, M. J. Han, N. Kobayashi, M. Ohfuti, F. Ishii, T. Ohwaki, H. Weng, and K. Terakura, <http://www.openmx-square.org/> (2009).
- [52] T. Ozaki, Variationally optimized atomic orbitals for large-scale electronic structures, *Phys. Rev. B* **67**, 155108 (2003).
- [53] T. Ozaki and H. Kino, Efficient projector expansion for the ab initio lcao method, *Phys. Rev. B* **72**, 045121 (2005).
- [54] J. P. Perdew, K. Burke, and M. Ernzerhof, Generalized gradient approximation made simple, *Phys. Rev. Lett.* **77**, 3865 (1996).
- [55] W. Kohn and L. J. Sham, Self-consistent equations including exchange and correlation effects,

- Phys. Rev. **140**, A1133 (1965).
- [56] T. Ozaki and H. Kino, Numerical atomic basis orbitals from h to kr, Phys. Rev. B **69**, 195113 (2004).
- [57] K. Lejaeghere, G. Bihlmayer, T. Björkman, P. Blaha, S. Blügel, V. Blum, D. Caliste, I. E. Castelli, S. J. Clark, A. Dal Corso, S. de Gironcoli, T. Deutsch, J. K. Dewhurst, I. Di Marco, C. Draxl, M. Dulak, O. Eriksson, J. A. Flores-Livas, K. F. Garrity, L. Genovese, P. Giannozzi, M. Giantomassi, S. Goedecker, X. Gonze, O. Grånäs, E. K. U. Gross, A. Gulans, F. Gygi, D. R. Hamann, P. J. Hasnip, N. A. W. Holzwarth, D. Iuşan, D. B. Jochym, F. Jollet, D. Jones, G. Kresse, K. Koepnik, E. Küçükbenli, Y. O. Kvashnin, I. L. M. Locht, S. Lubeck, M. Marsman, N. Marzari, U. Nitzsche, L. Nordström, T. Ozaki, L. Paulatto, C. J. Pickard, W. Poelmans, M. I. J. Probert, K. Refson, M. Richter, G.-M. Rignanese, S. Saha, M. Scheffler, M. Schlipf, K. Schwarz, S. Sharma, F. Tavazza, P. Thunström, A. Tkatchenko, M. Torrent, D. Vanderbilt, M. J. van Setten, V. Van Speybroeck, J. M. Wills, J. R. Yates, G.-X. Zhang, and S. Cottenier, Reproducibility in density functional theory calculations of solids, Science **351**, 10.1126/science.aad3000 (2016).
- [58] G. Henkelman and H. Jónsson, Improved tangent estimate in the nudged elastic band method for finding minimum energy paths and saddle points, The Journal of Chemical Physics **113**, 9978 (2000), <https://doi.org/10.1063/1.1323224>.
- [59] R. D. King-Smith and D. Vanderbilt, Theory of polarization of crystalline solids, Phys. Rev. B **47**, 1651 (1993).
- [60] G. Theurich and N. A. Hill, Self-consistent treatment of spin-orbit coupling in solids using relativistic fully separable ab initio pseudopotentials, Phys. Rev. B **64**, 073106 (2001).
- [61] H. Kotaka, F. Ishii, and M. Saito, Rashba effect on the structure of the bi one-bilayer film: Fully relativistic first-principles calculation, Japanese Journal of Applied Physics **52**, 035204 (2013).
- [62] M. A. U. Absor, I. Santoso, N. Yamaguchi, and F. Ishii, Spin splitting with persistent spin textures induced by the line defect in the $1t$ phase of monolayer transition metal dichalcogenides, Phys. Rev. B **101**, 155410 (2020).
- [63] M. A. U. Absor, I. Santoso, Harsojo, K. Abraha, H. Kotaka, F. Ishii, and M. Saito, Strong rashba effect in the localized impurity states of halogen-doped monolayer ptse_2 , Phys. Rev. B **97**, 205138 (2018).

- [64] M. A. U. Absor, I. Santoso, Harsojo, K. Abraha, H. Kotaka, F. Ishii, and M. Saito, Polarity tuning of spin-orbit-induced spin splitting in two-dimensional transition metal dichalcogenides, *Journal of Applied Physics* **122**, 153905 (2017), <https://doi.org/10.1063/1.5008475>.
- [65] J. H. Garcia, M. Vila, C.-H. Hsu, X. Waintal, V. M. Pereira, and S. Roche, Canted persistent spin texture and quantum spin hall effect in wTe_2 , *Phys. Rev. Lett.* **125**, 256603 (2020).
- [66] X. Kong, J. Deng, L. Li, Y. Liu, X. Ding, J. Sun, and J. Z. Liu, Tunable auxetic properties in group-iv monochalcogenide monolayers, *Phys. Rev. B* **98**, 184104 (2018).
- [67] B. Liu, M. Niu, J. Fu, Z. Xi, M. Lei, and R. Quhe, Negative poisson's ratio in puckered two-dimensional materials, *Phys. Rev. Materials* **3**, 054002 (2019).
- [68] J. H. Haeni, P. Irvin, W. Chang, R. Uecker, P. Reiche, Y. L. Li, S. Choudhury, W. Tian, M. E. Hawley, B. Craigo, A. K. Tagantsev, X. Q. Pan, S. K. Streiffer, L. Q. Chen, S. W. Kirchoefer, J. Levy, and D. G. Schlom, Room-temperature ferroelectricity in strained SrTiO_3 , *Nature* **430**, 758 (2004).
- [69] S. Ok, L. Muechler, D. Di Sante, G. Sangiovanni, R. Thomale, and T. Neupert, Custodial glide symmetry of quantum spin hall edge modes in monolayer wTe_2 , *Phys. Rev. B* **99**, 121105 (2019).
- [70] L.-k. Shi and J. C. W. Song, Symmetry, spin-texture, and tunable quantum geometry in a wTe_2 monolayer, *Phys. Rev. B* **99**, 035403 (2019).
- [71] S.-Y. Xu, Q. Ma, H. Shen, V. Fatemi, S. Wu, T.-R. Chang, G. Chang, A. M. M. Valdivia, C.-K. Chan, Q. D. Gibson, J. Zhou, Z. Liu, K. Watanabe, T. Taniguchi, H. Lin, R. J. Cava, L. Fu, N. Gedik, and P. Jarillo-Herrero, Electrically switchable berry curvature dipole in the monolayer topological insulator wTe_2 , *Nature Physics* **14**, 900 (2018).
- [72] N. Ding, J. Chen, C. Gui, H. You, X. Yao, and S. Dong, Phase competition and negative piezoelectricity in interlayer-sliding ferroelectric ZrI_2 , *Phys. Rev. Materials* **5**, 084405 (2021).
- [73] T. Zhang, Y. Liang, X. Xu, B. Huang, Y. Dai, and Y. Ma, Ferroelastic-ferroelectric multiferroics in a bilayer lattice, *Phys. Rev. B* **103**, 165420 (2021).
- [74] X. Liu, A. P. Pyatakov, and W. Ren, Magnetoelectric coupling in multiferroic bilayer vs_2 , *Phys. Rev. Lett.* **125**, 247601 (2020).